electronics

MDPI

Article

Design of an E-Band Multiplexer Based on Turnstile Junction

Shaohang Li, Yuan Yao *, Xiaohe Cheng and Junsheng Yu

School of Electronic Engineering, Beijing University of Posts and Telecommunications, Beijing 100876, China; lishaohang@bupt.cn (S.L.); xiaohec@bupt.edu.cn (X.C.); jsyu@bupt.edu.cn (J.Y.)
* Correspondence: yaoy@bupt.edu.cn

Abstract: This paper presents an E-band four-channel multiplexer based on a turnstile junction. The proposed multiplexer consists of a power distribution unit featuring a turnstile junction topology and four Chebyshev bandpass filters. Thanks to the implementation of a rotating gate connection structure as the distribution unit, the overall compactness was enhanced, and the complexity of optimization was significantly reduced. Furthermore, this configuration offers a well-organized spatial port distribution, facilitating scalability for additional channels. According to the frequency band planning and design requirements of the communication system, an E-band four-channel multiplexer was designed and manufactured using high-precision computer numerical control (CNC) milling technology, achieving an error margin of ±5 μm. The experimental results indicate that the passbands are 70.6–73.07 GHz, 73.7–76.07 GHz, 82.55–82.9 GHz, and 83.4–85.9 GHz. The in-band insertion loss of each channel is below 1.7 dB, while the return loss at the common port exceeds 12 dB. The measured results align closely with simulations, demonstrating promising potential for practical applications.

Keywords: bandpass filter; E-band multiplexer; power distribution; turnstile junction; waveguide technology

1. Introduction

With the advancement of electronic technology, the demand for communication rates has exceeded 10 Gbps. To achieve higher transmission rates, communication systems must either have a larger absolute bandwidth or utilize higher-order modulation techniques to improve spectrum efficiency. However, the lower-frequency microwave bands in the radio spectrum have become saturated. In contrast, the millimeter-wave frequency band offers abundant resources that can effectively address the issue of an insufficient low-frequency bandwidth, facilitating the implementation of high-speed wireless communication systems [1–3]. Furthermore, due to its position within the atmospheric window, the E-band experiences lower atmospheric attenuation, making it the most promising millimeter-wave band for various applications [4–6]. Currently, the 71–76/81–86 GHz frequency band is designated for communication links between satellites and the ground, as well as for 5G network development, with a typical available bandwidth of 500–2000 MHz [7,8].

In response to the demand for higher transmission rates, multiple subchannels are often employed for link aggregation to achieve a greater overall bandwidth. Consequently, it is essential to utilize a multiplexer to decompose and combine sub-signals of varying frequencies. Additionally, due to the high frequency of millimeter waves, the dielectric loss in the components is relatively significant. Therefore, compared to microstrip lines [9–11], substrate integrated waveguides (SIW) [12–16], and other types of multiplexers, the use

check for updates

Received: 27 January 2025
Revised: 5 March 2025
Accepted: 5 March 2025
Published: 7 March 2025

Citation: Li, S.; Yao, Y.; Cheng, X.; Yu, J. Design of an E-Band Multiplexer Based on Turnstile Junction. *Electronics* **2025**, *14*, 1072. https://doi.org/10.3390/electronics14061072

of air cavities devoid of dielectric materials in multiplexer design provides a substantial advantage in terms of low insertion loss.

Air-filled cavity multiplexers are typically implemented using gap waveguides [17–19] or air waveguides [20–27]. The gap waveguide structure leverages artificial magnetic surfaces to support electromagnetic wave propagation while maintaining an air gap, thereby improving assembly tolerance [28]. For instance, Ref. [17] presents a K/Ka-band diplexer that integrates a simplified rotary joint with multi-mode cavity operation, whereas [18] introduces a V-band diplexer based on Chebyshev bandpass filters and a T-junction power-divider. While these designs demonstrate favorable electrical performance, their limited number of channels increases the structural complexity and manufacturing challenges as the number of channels grows. Recent advancements in machining precision and assembly techniques have further emphasized the compactness and efficiency of air-filled metallic waveguides, particularly for multi-channel multiplexer designs.

Using a hybrid coupler as the primary component for channel isolation and power distribution, an identical filter can be connected to the power distribution ports while another passband filter is attached to the isolation port. This configuration effectively separates signals of different frequencies. However, as the channel count increases, the complexity of the multiplexer significantly escalates. In contrast, manifold waveguides [22–27] provide an alternative approach by achieving the initial frequency selection through adjustments in arm length and channel spacing, followed by further optimization to enhance return loss. While this method promotes structural simplicity and manufacturability, the planar port distribution may require additional conversion structures for system-level integration.

In order to address these challenges, this paper proposes a compact and efficient multiplexer design based on a turnstile junction. The proposed structure features a streamlined optimization process and a practical physical configuration. The multiplexer utilizes a turnstile junction power distribution unit with bandpass filters connected to each output port. Designed for E-band communication systems, the multiplexer integrates four channels, covering passbands of 71–73 GHz, 74–76 GHz, 81–83 GHz, and 84–86 GHz, with a return loss target of over 15 dB. The design principles and implementation details are presented in the following sections.

2. Design Principles

2.1. Design of the Turnstile Junction

The turnstile junction, a waveguide-based structure, is employed in millimeter-wave component designs due to its high-power handling capability, low insertion loss, and excellent power distribution characteristics. Its relatively simple structure further enhances its applicability in high-frequency communication systems. The proposed design, illustrated in Figure 1, consists of five physical ports. The common port (Port 1) is positioned at a 45° angle relative to both the x-axis and y-axis. The four power distribution output ports (Ports 2–5) adopt WR-12 standard waveguide dimensions, with a length (a) and width (b) of 3.1 × 1.55 mm.

In order to enhance power distribution characteristics, a rectangular metallic post is positioned directly beneath Port 1. This post is perpendicularly aligned with the common port and functions as an adjustment mechanism. It has a length (l_t), width (w_t), and height (h_t), ensuring precise control of the power division and wave propagation properties. The integration of this structure allows for efficient signal distribution while maintaining a compact footprint, making it well-suited for millimeter-wave applications.

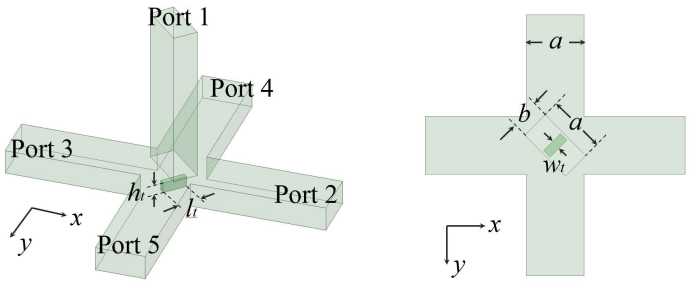

Figure 1. Physical structure and dimensions of the turnstile junction.

The turnstile junction can be functionally decomposed into two E-plane T-junctions, enabling four-way power distribution. The corresponding electric field distribution and schematic representation are illustrated in Figure 2. The electric field E at the common port (Port 1) can be decomposed into two orthogonal components, E_1, which is parallel to the $-y$-axis, and E_2, which is parallel to the x-axis. To maintain equal power of the four output ports, the electric fields E_1 and E_2 should remain the same, which can be achieved by rotating Port 1 by 45°. Consequently, the electric field component E_1 interacts with Port 4 and Port 5, forming one T-junction structure, while E_2 interacts with Port 2 and Port 3, forming another independent T-junction. Since these two T-junctions are orthogonally aligned, they operate independently, thereby preventing signal interference between the two pathways.

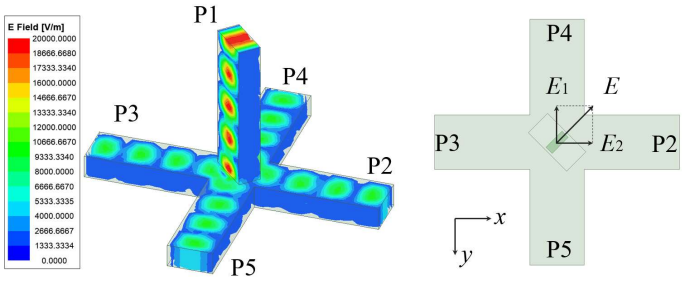

Figure 2. Electric field distributions and schematic diagram of the turnstile junction.

Based on the above analysis, the energy transmission model of this structure can be equivalently represented as a reciprocal six-port network. The corresponding schematic diagram is illustrated in Figure 3, and its S-parameter matrix is given in Equation (1):

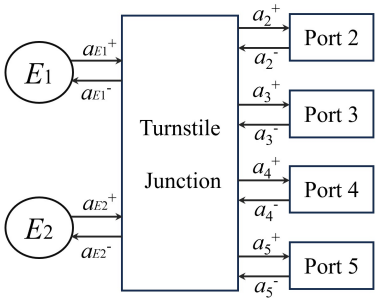

Figure 3. Schematic diagram of energy transmission in the turnstile junction. The a_{Ei}^+ and a_{Ei}^- represent the input E-field intensity and the output E-field intensity of Port 1, respectively. (i = 1, 2). The a_j^+ and a_j^- represent the output E-field intensity and the input E-field intensity of Port j, respectively. (j = 2, 3, 4, 5).

$$[S] = \frac{1}{2} \cdot \begin{bmatrix} & E_1 & E_2 & \text{P2} & \text{P3} & \text{P4} & \text{P5} \\ E_1 & 0 & 0 & 0 & 0 & -\sqrt{2} & \sqrt{2} \\ E_2 & 0 & 0 & \sqrt{2} & -\sqrt{2} & 0 & 0 \\ \text{P2} & 0 & \sqrt{2} & 1 & 1 & 0 & 0 \\ \text{P3} & 0 & -\sqrt{2} & 1 & 1 & 0 & 0 \\ \text{P4} & -\sqrt{2} & 0 & 0 & 0 & 1 & 1 \\ \text{P5} & \sqrt{2} & 0 & 0 & 0 & 1 & 1 \end{bmatrix} \quad (1)$$

Taking the T-junction excited by E_1 as an example, when Port 4 is used as the excitation port, both Port 5 and E_1 receive energy. Similarly, when Port 5 serves as the excitation port, power is also distributed to Port 4 and E_1. However, when excitation is applied through E_1, the structural symmetry of Port 4 and Port 5 with respect to the central symmetry plane, combined with the anti-symmetric electric field distribution of E_1, results in equal-amplitude but phase-opposite signals at Port 4 and Port 5, equidistant from the symmetry plane.

Finally, to evaluate and optimize the turnstile junction model based on equal power-splitting, numerical simulations were conducted. The preliminary results, as illustrated in Figure 4, indicate that within the 65–90 GHz frequency range, the return loss remains better than −18 dB, the transmission coefficients at all ports exceed −6.2 dB, and the port balance at identical frequency points is maintained within 0.25 dB. These results demonstrate the excellent power distribution performance.

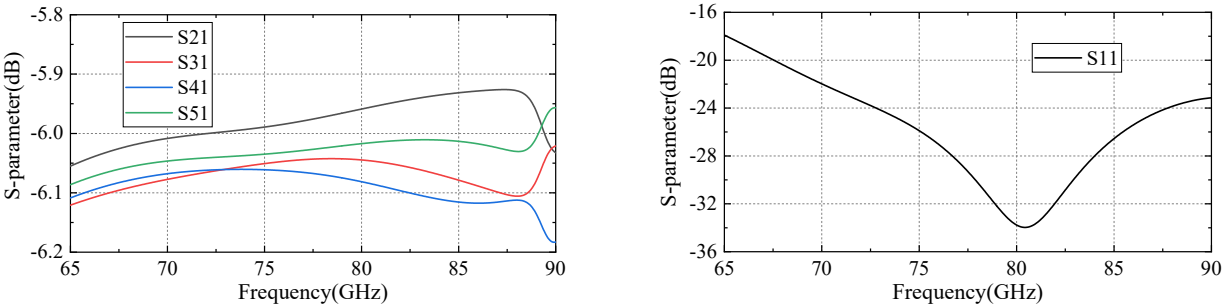

Figure 4. Simulated S-parameter results of the turnstile junction.

2.2. Design of the Bandpass Filter

In order to balance frequency selectivity and design complexity, a fourth-order Chebyshev bandpass filter based on a metallic waveguide cavity was selected for this design. According to the communication band allocation rules, the designated passbands for the four channels were 71–73 GHz, 74–76 GHz, 81–83 GHz, and 84–86 GHz.

As illustrated in Figure 5, the proposed bandpass filter consists of four rectangular resonant cavities, which are coupled through inductive coupling windows. The filter exhibits a symmetric structure. The resonant frequency calculation equation of cavity is given in Equation (2); the c is the speed of light, the a and l represent the width and length of the cavity, respectively.

$$f_c = \frac{c}{2}\sqrt{\left(\frac{1}{a}\right)^2 + \left(\frac{1}{l}\right)^2} \quad (2)$$

The actual coupling coefficient m can be calculated using Equation (3). With a return loss requirement of better than 20 dB, the normalized coupling coefficients are determined as $M_{S1} = M_{4L} = 1.035$, $M_{12} = M_{34} = 0.911$, and $M_{23} = 0.7$.

$$m_{ij} = M_{ij} \cdot BW \quad (3)$$

where i, j = S, 1, 2, 3, 4, L; BW is the relative bandwidth. Based on the coupling theory for bandpass filters [29], the value of the coupling coefficients and Qex is given in Table 1.

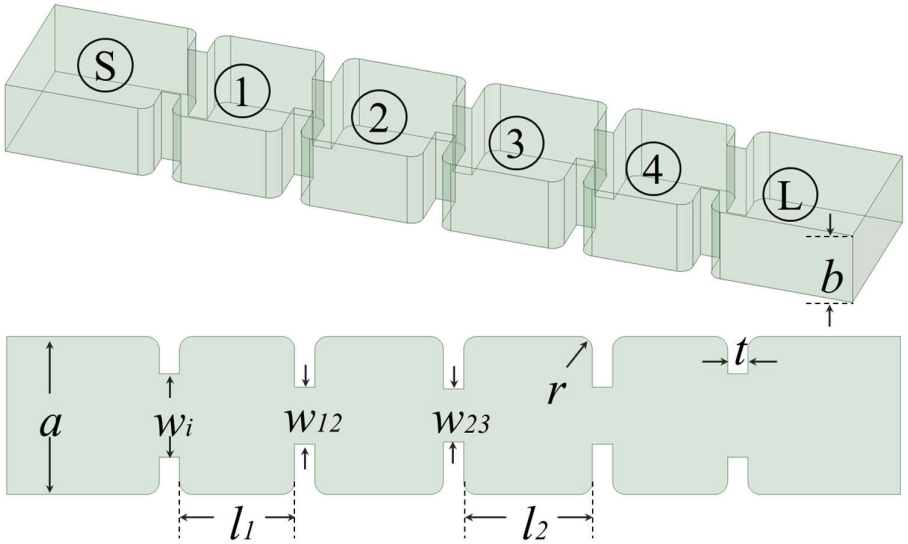

Figure 5. Physical structure and dimensions of the bandpass filter.

Table 1. The value of the coupling coefficients and Qex of each bandpass filter.

	BW	m_{S1}/m_{4L}	m_{12}/m_{34}	m_{23}	Q_{ex}
BPF1	2.78%	0.0288	0.0253	0.0194	33.59
BPF2	2.67%	0.0276	0.0243	0.0187	34.99
BPF3	2.44%	0.0252	0.0222	0.017	38.26
BPF4	2.35%	0.0244	0.0214	0.0165	39.66

The simulated results of the coupling coefficients and external quality factor (Q_{ex}) are presented in Figure 6. Figure 6a shows the effects of w_{12} on the coupling coefficients given by the eigenmode in HFSS. The simulation model utilizes the Perfect Electric Conductor (PEC) as the boundary and solves the two resonant frequencies f_1 and f_2. The coupling coefficients equation is shown in Equation (4).

$$m = \left| \frac{f_2^2 - f_1^2}{f_2^2 + f_1^2} \right| \tag{4}$$

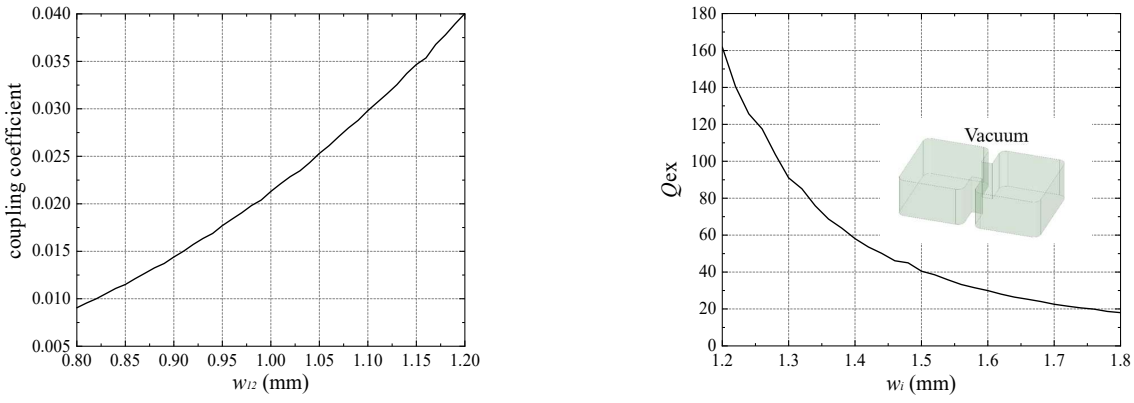

Figure 6. (**a**) Effects of w_{12} on the coupling coefficient; (**b**) effects of w_i on Q_{ex}.

The effects of the w_i on Qex given by the driven mode in HFSS are shown in Figure 6b. The PEC boundary is adopted and the group delay characteristics are solved. The relationship between the maximum group delay t and frequency f_0 is shown in by Equation (5).

$$Q_{\text{ex}} = \frac{\pi f_0 t}{2} \tag{5}$$

As the size of the coupling window increases, the coupling coefficient correspondingly increases, while Qex decreases.

By optimizing the dimensions of cavities a, l, and coupling coefficient m, the final parameters of the proposed multiplexer are determined. The dimensions and corresponding simulation results of the filters are presented in Table 2 and Figure 7. The obtained passband bandwidths are 70.9–73.08 GHz, 73.92–76.1 GHz, 80.92–83.08 GHz, and 83.9–86.14 GHz, respectively. In all cases, the return loss is better than 20 dB, demonstrating compliance with the expected design specifications.

Table 2. Dimensions of each bandpass filter (units in millimeters).

	BPF1	**BPF 2**	**BPF 3**	**BPF 4**
Passband (GHz)	71–73	74–76	81–83	84–86
a	3.1	3.1	3.1	3.1
b	1.55	1.55	1.55	1.55
t	0.4	0.4	0.4	0.4
r	0.25	0.25	0.25	0.25
w_{i}	1.64	1.57	1.44	1.41
l_1	2.263	2.116	1.854	1.748
l_2	2.532	2.365	2.064	1.953
w_{12}	1.117	1.055	0.951	0.926
w_{23}	1.042	0.982	0.888	0.862

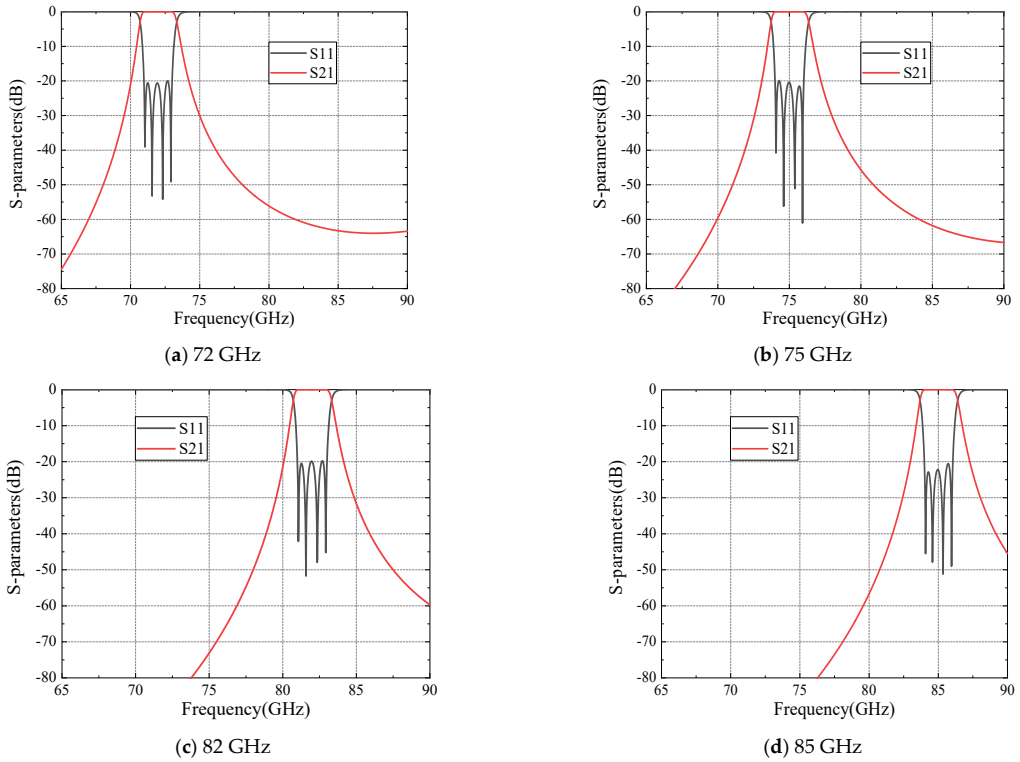

(**a**) 72 GHz (**b**) 75 GHz

(**c**) 82 GHz (**d**) 85 GHz

Figure 7. Simulation results of each bandpass filter.

2.3. Design of the Turnstile Multiplexer

The final design of the multiplexer is achieved by connecting each bandpass filter to the four power distribution ports of the turnstile junction using stubs with different arm lengths. As illustrated in Figure 8, the stub lengths are denoted as *li_chn* (n = 1, 2, 3, 4), with their initial values set to approximately $m\lambda_g/2$ (where λ_g is the guided wavelength and m is a constant) for further optimization. Additionally, to enhance the adjustability of the multiplexer, the rotation angle (θ) between the common port and the metallic ridge is introduced as a tunable parameter, allowing for the power distribution among the output ports to be fine-tuned.

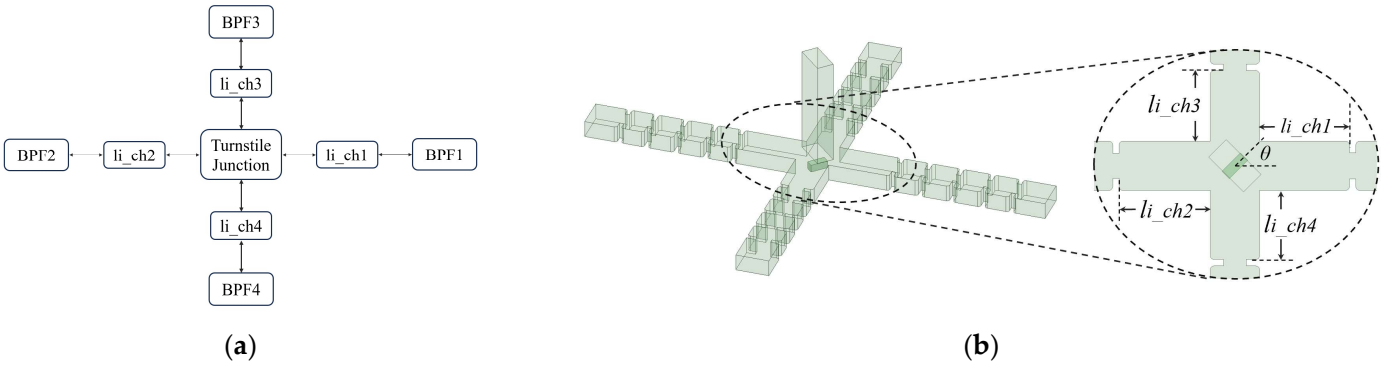

(**a**) (**b**)

Figure 8. (**a**) Distributed model and (**b**) physical structure and dimensions of the turnstile junction multiplexer.

Although the individual bandpass filters optimized in the previous section exhibit excellent channel responses, the turnstile junction lacks complete directivity and isolation properties, leading to interactions between different channels that degrade the overall multiplexer performance. Therefore, it is necessary to optimize the distributed model to meet the design specifications. The optimization process can be summarized as follows:

(1) Optimization of the stub lengths between the turnstile junction and each bandpass filter, as well as the dimensions of the metallic post within the junction. This step is particularly critical for enhancing the common-port return loss (CPRL) performance.
(2) Fine-tuning the parameters of each bandpass filter individually to adjust the passband frequencies and further improve the filtering characteristics.
(3) Iteratively refining the optimization process by increasing the number of design variables or integrating multiple objectives into the optimization framework until the desired response is achieved.

The simulation-based optimization results, presented in Figure 9, demonstrate that the passbands of the four output ports are 70.78–73.25 GHz, 73.85–76.14 GHz, 80.84–83.02 GHz, and 83.86–86.32 GHz, respectively. Within these passbands, the return loss remains better than 15 dB, indicating excellent electrical performance. Additionally, the electric field distributions of the turnstile junction multiplexer at different frequencies are illustrated in Figure 10.

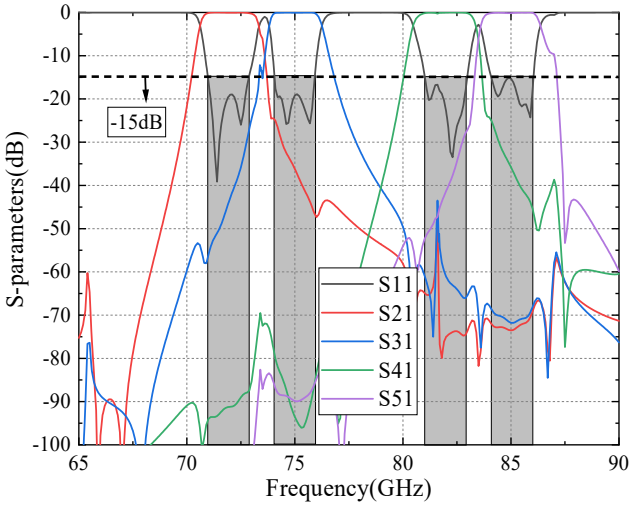

Figure 9. Simulated S-parameter results of the turnstile junction multiplexer.

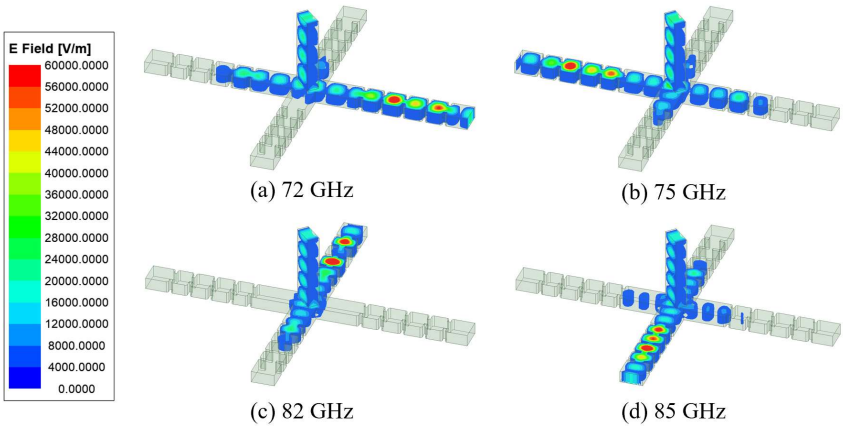

Figure 10. The electric field distribution at different frequencies.

3. Fabrication and Measurement

In order to meet the fabrication and testing requirements, the UG387 flanges and WR12 standard waveguide ports were used as the test interfaces for all ports. Additionally, the model was divided into two layers for fabrication. The cavity structures of the bandpass filters and the metallic post of the turnstile junction were machined on the bottom layer using computer numerical control (CNC) milling, while the waveguide structure of the common port was processed using CNC wire electrical discharge machining (wire EDM). A slot-based alignment mechanism was incorporated between the two layers to minimize assembly errors. The final structural design of the turnstile junction multiplexer is shown in Figure 11.

The fabricated prototype and testing setup are presented in Figure 12. The entire structure is made of aluminum. The performance evaluation was conducted using a 3672E vector network analyzer (VNA) from CETC in Qingdao, China, in combination with a 3644 N frequency extension module. The test interfaces were extended via WR12 waveguides, and the multiplexer was subsequently tested. The performance of the proposed filter is shown in Figure 13, indicating that the passbands are 70.6–73.07 GHz, 73.7–76.07 GHz, 82.55–82.9 GHz, and 83.4–85.9 GHz. Figure 13 shows that the maximum in-band insertion loss is approximately 1.7 dB, while the return loss remains better than 12 dB. Besides, the adjacent port-to-port isolations of S32 and S43 are better than 20 dB, and those of other isolations, S52 and S54, are better than 60 dB.

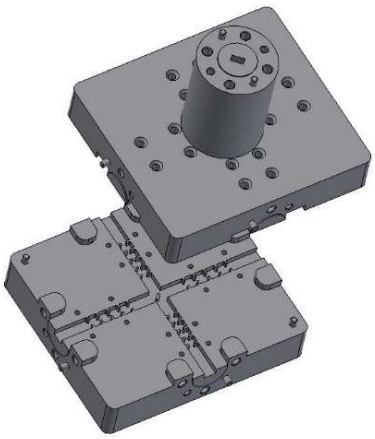

Figure 11. The fabrication model of the turnstile junction multiplexer.

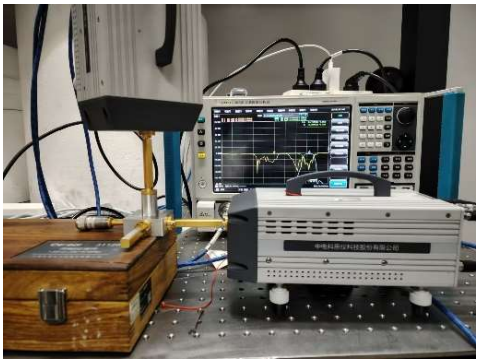

Figure 12. The fabricated prototype and test scenario.

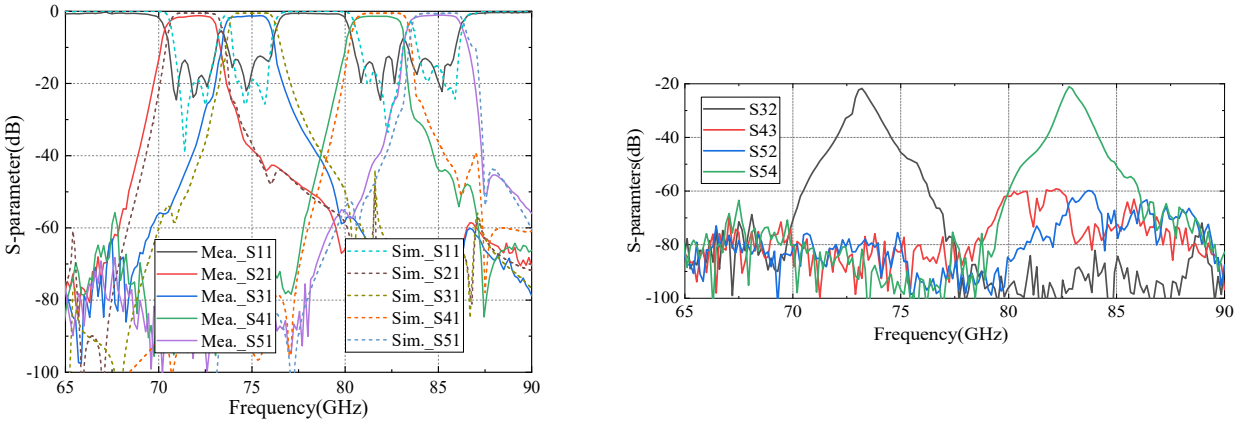

Figure 13. The simulated and measured results of the turnstile junction multiplexer.

Compared to the simulation results, the measured passband frequencies exhibit a downward shift, and the insertion loss is higher. This discrepancy is likely attributed to fabrication tolerances and surface roughness in the CNC machining process, which may have introduced air gaps between the upper and lower layers of the model, leading to electromagnetic wave leakage and increased insertion loss.

The comparison between the proposed turnstile junction multiplexer and other reported multiplexers is shown in Tables 3 and 4. Compared with [13,14], the proposed filter has the advantage of a lower IL. Compared with [17,18], the implementation of multi-channel multiplexers was achieved. Compared with [18,25], the proposed filter exhibits broadband characteristics. The proposed novel multiplexer exhibits a supe-

rior electrical performance, providing an innovative solution for the implementation of multi-channel multiplexers.

Table 3. Final dimensions of the turnstile junction multiplexer (units in millimeters).

Parameters	CH1	CH2	CH3	CH4	Parameters	Value
Passband (GHz)	**71–73**	**74–76**	**81–83**	**84–86**		
l_i	2.23	2.272	1.044	0.65	T	0.4
w_i	1.64	1.6	1.46	1.42	R	0.25
l_1	2.263	2.095	1.843	1.744	w_t	0.66
l_2	2.532	2.37	2.062	1.954	l_t	1.623
w_{12}	1.117	1.068	0.966	0.93	h_t	0.7
w_{23}	1.042	0.976	0.899	0.857	Θ	43.25

Table 4. Comparison of the proposed and other reported multiplexers.

Reference	Operational Band (GHz)	IL (dB)	CPRL (dB)	MUX Type	Technology	No. of Channel
[13]	71–86	2	18	Hybrid-coupled	SIW	2
[14]	18–22	2.1	15	T-junction	SIW	4
[17]	18–32	0.9	15	Simplified rotary joint	CNC	2
[18] *	58–64	1	10	T-junction	CNC	2
[25]	200–225	1.7	15	Manifold	CNC	4
This work	**71–86**	**1.7**	**12**	**Turnstile junction**	**CNC**	**4**

* Indicates simulation results of an unfinished fabrication.

4. Conclusions

In this paper, a novel E-band multiplexer based on the turnstile junction is proposed, which differs from conventional multiplexer designs as it utilizes the turnstile junction as the core component for power distribution. By introducing only one turnstile to achieve four-way power division, the design and optimization of the multi-way power-divider can be simplified to that of the metal stub. In addition, since the adjacent output ports of the turnstile have orthogonal characteristics, the four-way design can be simplified to a two-way design. In order to validate the proposed design, the multiplexer was fabricated and experimentally tested. The measured passbands were 70.6–73.07 GHz, 73.7–76.07 GHz, 82.55–82.9 GHz, and 83.4–85.9 GHz. The in-band insertion loss for each channel remained below 1.7 dB, while the common-port return loss was better than 12 dB. The measured results closely align with the simulation results, demonstrating the effectiveness and reliability of the proposed approach. Given its superior electrical performance and promising application prospects, this design methodology offers a viable solution for multiplexer development in multi-frequency communication systems.

Author Contributions: Conceptualization, S.L. and Y.Y.; methodology, S.L.; formal analysis, S.L.; investigation, X.C. and J.Y.; writing—original draft preparation, S.L.; writing—review and editing, Y.Y. and X.C. All authors have read and agreed to the published version of the manuscript.

Funding: This research received no external funding.

Data Availability Statement: Data are contained within the article.

Conflicts of Interest: The authors declare no conflicts of interest.

References

1. Pi, Z.; Khan, F. An introduction to millimeter-wave mobile broadband systems. *IEEE Commun. Mag.* **2011**, *49*, 101–107. [CrossRef]
2. Wang, P.; Li, Y.; Song, L.; Vucetic, B. Multi-gigabit millimeter wave wireless communications for 5G: From fixed access to cellular networks. *IEEE Commun. Mag.* **2015**, *53*, 168–178. [CrossRef]
3. Jiang, H.; Wang, C.; Xiu, T.; Wang, D.; Hu, S.; Zhan, X.; Yu, J.; Chen, X.; Yao, Y. High speed wireless communication system at W-band. In Proceedings of the International Conference on Microwave and Millimeter Wave Technology (ICMMT), Guangzhou, China, 19–22 May 2019; pp. 1–3.
4. Schneider, T.; Wiatrek, A.; Preussler, S.; Grigat, M.; Braun, R.-P. Link Budget Analysis for Terahertz Fixed Wireless Links. *IEEE Trans. Terahertz Sci. Technol.* **2012**, *2*, 250–256. [CrossRef]
5. Jang, K.J.; Oh, J.H.; Yoon, Y.; Kim, J.; Hwang, G. Atmospheric Attenuation Model Using Gaussian Process in Sub-THz Terrestrial Wireless Communications. *IEEE Antennas Wirel. Propag. Lett.* **2024**, *23*, 568–572. [CrossRef]
6. Manoliu, L.; Henneberger, R.; Tessmann, A.; Seidel, J.; Eppard, M.; Kallfass, I. Impairments of Atmospheric Attenuation on a Wideband E-Band Outdoor Communication Link. In Proceedings of the 2021 51st European Microwave Conference (EuMC), London, UK, 4–6 April 2022.
7. Luini, L.; Roveda, G.; Zaffaroni, M.; Costa, M.; Riva, C.G. The Impact of Rain on Short E -Band Radio Links for 5G Mobile Systems: Experimental Results and Prediction Models. *IEEE Trans. Antennas Propag.* **2020**, *68*, 3124–3134. [CrossRef]
8. Harati, P.; Schoch, B.; Tessmann, A.; Schwantuschke, D.; Henneberger, R.; Czekala, H.; Zwick, T.; Kallfass, I. Is E-Band Satellite Communication Viable?: Advances in Modern Solid-State Technology Open Up the Next Frequency Band for SatCom. *IEEE Microw. Maga.* **2017**, *18*, 64–76. [CrossRef]
9. Zheng, T.; Wei, B.; Cao, B.; Guo, X.; Zhang, X.; Jiang, L.; Xu, Z.; Heng, Y. Compact Superconducting Diplexer Design With Conductor-Backed Coplanar Waveguide Structures. *IEEE Trans. Appl. Supercond.* **2015**, *25*, 1501304. [CrossRef]
10. Hong, S.; Chang, K. Stub-tuned microstrip bandpass filters for millimeter-wave diplexer design. *IEEE Microw. Wirel. Compon. Lett.* **2005**, *15*, 582–584. [CrossRef]
11. Gómez-García, R.; Yang, L.; Munoz-Ferreras, J.-M. Balanced Quasi-Elliptic-Type Combline Diplexer With Multiextracted-Pole Junction/Output Sections. *IEEE Microw. Wirel. Compon. Lett.* **2020**, *30*, 569–572. [CrossRef]
12. Zhou, K.; Wu, K. Substrate Integrated Waveguide Multiband Bandpass Filters and Multiplexers: Current Status and Future Outlook. *IEEE J. Microw.* **2023**, *3*, 466–483. [CrossRef]
13. Uemichi, Y.; Nukaga, O.; Han, X.; Amakawa, S.; Guan, N. Highly Configurable Cylindrical-Resonator-Based Bandpass Filter Built of Silica-Based Post-Wall Waveguide and Its Application to Compact E-Band Hybrid-Coupled Diplexer. In Proceedings of the 2019 IEEE MTT-S International Microwave Symposium (IMS), Boston, MA, USA, 2–7 June 2019.
14. Su, Z.L.; Xu, B.W.; Zheng, S.Y.; Liu, H.W.; Long, Y.L. High-Isolation and Wide-Stopband SIW Diplexer Using Mixed Electric and Magnetic Coupling. *IEEE Trans. Circuits Syst. II Express Briefs* **2020**, *67*, 32–36. [CrossRef]
15. Hao, Z.-C.; Huo, X.-P.; Ding, W.-Q.; Hong, W. Efficient Design of Compact Contiguous-Channel SIW Multiplexers Using the Space-Mapping Method. *IEEE Trans. Microw. Theory Tech.* **2015**, *63*, 3651–3662. [CrossRef]
16. Ma, D.; Zhou, K.; Xie, H.; Huang, T.; Wu, W. Compact or Wide-Stopband SIW Diplexers with High Intrinsic Isolations Based on Orthogonal Dual Modes. *IEEE Trans. Circuits Syst. II Express Briefs* **2023**, *70*, 71–75. [CrossRef]
17. Lin, Y.; You, Y.; Shen, S.; Huang, J.; Lu, Y. A K-/Ka-Band Diplexer-Integrated Simplified Rotary Joint Using Gap Waveguide Technology. *IEEE Microw. Wirel. Technol. Lett.* **2023**, *33*, 1139–1142. [CrossRef]
18. Rezaee, M.; Zaman, A.U.; Kildal, P.-S. V-band groove gap waveguide diplexer. In Proceedings of the 2015 9th European Conference on Antennas and Propagation (EuCAP), Lisbon, Portugal, 13–17 April 2015.
19. Huang, R.; Wu, Y.; Ran, J.; Wu, L.; Meng, F.; Wang, W. Low Insertion Loss and High Isolation Gap Waveguide Diplexer for Ka-Band Satellite Communication Links. In Proceedings of the 2024 International Conference on Microwave and Millimeter Wave Technology (ICMMT), Bejing, China, 16–19 May 2024.
20. Kojima, T.; Gonzalez, A.; Asayama, S.; Uzawa, Y. Design and Development of a Hybrid-Coupled Waveguide Multiplexer for a Multiband Receiver. *IEEE Trans. Terahertz Sci. Technol.* **2017**, *7*, 10–19. [CrossRef]
21. Gonzalez, A.; Kojima, T.; Kaneko, K.; Asayama, S. 275–500 GHz Waveguide Diplexer to Combine Local Oscillators for Different Frequency Bands. *IEEE Trans. Terahertz Sci. Technol.* **2017**, *7*, 669–676. [CrossRef]
22. Montejo-Garai, J.R.; Ruiz-Cruz, J.A.; Rebollar, J.M. Full-wave design of H-plane contiguous manifold output multiplexers using the fictitious reactive load concept. *IEEE Trans. Microw. Theory Tech.* **2005**, *53*, 2628–2632. [CrossRef]
23. Cameron, R.I.; Yu, M. Design of manifold-coupled multiplexers. *IEEE Microw. Mag.* **2007**, *8*, 46–59. [CrossRef]
24. Carceller, C.; Soto, P.; Boria, V.; Guglielmi, M.; Gil, J. Design of Compact Wideband Manifold-Coupled Multiplexers. *IEEE Trans. Microw. Theory Tech.* **2015**, *63*, 3398–3407. [CrossRef]
25. Feng, Y.; Zhang, B.; Liu, Y.; Niu, Z.; Dai, B.; Fan, Y.; Chen, X. A 200–225-GHz Manifold-Coupled Multiplexer Utilizing Metal Waveguides. *IEEE Trans. Microw. Theory Tech.* **2021**, *69*, 5327–5333. [CrossRef]

26. Holloway, J.W.; Dogiamis, G.C.; Shin, S.; Han, R. 220-to-330-GHz Manifold Triplexer with Wide Stopband Utilizing Ridged Substrate Integrated Waveguides. *IEEE Trans. Microw. Theory Tech.* **2020**, *68*, 3428–3438. [CrossRef]
27. Feng, Y.; Zhang, B.; Liu, Y.; Niu, Z.; Fan, Y.; Chen, X. A D-Band Manifold Triplexer With High Isolation Utilizing Novel Waveguide Dual-Mode Filters. *IEEE Trans. Terahertz Sci. Technol.* **2022**, *12*, 678–681. [CrossRef]
28. Kildal, P.-S.; Alfonso, E.; Valero-Nogueira, A.; Rajo-Iglesias, E. Local Metamaterial-Based Waveguides in Gaps Between Parallel Metal Plates. *IEEE Antennas Wirel. Propag. Lett.* **2009**, *8*, 84–87. [CrossRef]
29. Pozar, D.M. *Microwave Engineering*; J. WILEY: Hoboken, NJ, USA, 2006.